ISAR Imaging and Scaling Method of Precession Targets in Wideband T/R-R Bistatic Radar

Xiaofeng Ai[*]**, Yonghu Zeng, Liandong Wang, Manxi Wang, and Yongzhen Li**

Abstract—Imaging and scaling of precession targets are very important in spatial target surveillance. The bistatic wideband radar echo model of the spatial precession cone-shaped target is induced, and bistatic ISAR imaging method based on time-frequency analysis is described. Combined with the monostatic and bistatic scattering characteristics of cone-shaped targets, the cross scaling method is presented through range instantaneous Doppler (RID) image matching using T/R-R bistatic radar observations, and the correct scaled monostatic and bistatic two-dimensional images can be obtained at the same time, which can reflect the actual size of the target. The algorithm is validated by dynamic simulation with electromagnetic computation data and provides a feasible way for the stable recognition of spatial targets.

1. INTRODUCTION

Precession is a typical micro-motion of ballistic targets [1] and widely used for ballistic mid course target parameter estimation, imaging and recognition. Ref. [2] introduces the ballistic target imaging and feature extraction method based on micro-motion systematically. The ballistic missile attack and defense is becoming increasingly fierce, and the jamming and deception are more and more complex, which provides increasingly serious challenges for monostatic radar. Bi-/multistatic radar has many advantages over monostatic radar: separated transmitter and receiver configurations offer the ability to detect stealthy targets and offer immunity to jamming; multistatic radar achieves spatially diverse geometries to observe threats and countermeasures from multiple viewing angles and provide high-detection performance. So Bi-/multistatic radar regains much more concern [3–6].

In recent years, bistatic ISAR has become a hot research topic. Refs. [7] and [8] research the basic principle of bistatic ISAR imaging and analyze its resolution; Refs. [9] and [10] research bistatic range-Doppler (RD) imaging method, and proposed an adaptive focusing method which is also robust under the condition of phase synchronization error. Ref. [11] study on the fusion imaging using the multi-aspect observation, which can shorten imaging time and improve the cross resolution. However, all the study uses the ideal scattering point model and ignore the differences of the bistatic scattering characteristics of target which makes the bistatic imaging results far from target recognition.

Micro-Doppler produced by precession target is highly nonlinear, and the cross direction is difficult to focus if using the traditional RD imaging method, so the time-frequency analysis method can be used for range instantaneous Doppler (RID) imaging as [12]. The existing problem is that the cross direction is difficult to scale in the instantaneous Doppler, thus the RID images cannot be used directly for target recognition. The spatial targets always have the rotation symmetrical structure and Doctor Jin utilized two monostatic RID images for cross direction scaling via image match [13], where the key point is to find two RID images with large attitude difference in monostatic radar observations. However, in

practice the precession angle of targets are usually small, and the attitude difference is also small, so it will greatly reduce the possibility of scaling and precision. Using T/R-R bistatic radar observations, two RID images can be obtained at the same time, both of which can be scaled using the rotation symmetry characteristics, and it is not limited by the small target attitude variation.

The remainder of this paper is organized as follows. Section 2 establishes wideband bistatic radar echo model of precession target. Section 3 presents the bistatic RID imaging method based on time-frequency analysis and describes the scaling method of monostatic and bistatic RID images using the target rotation symmetry characteristics. Section 4 simulates the monostatic and bistatic RID images of precession targets with electromagnetic calculation data and validates the proposed method. Section 5 concludes this paper.

2. WIDEBAND BISTATIC RADAR ECHO MODEL OF PRECESSION TARGET

As shown in Fig. 1, the bistatic scattering field of the cone-shaped target is contributed by scattering center A on the top and scattering centers B and C at the intersection of the bottom edge and the plane that is constructed by the symmetry axis and the bisector of the bistatic angle [14] The monostatic scattering field is contributed by scattering centers A, D, and E Scattering centers D and E are at the intersection of the bottom edge and the plane constructed by the symmetry axis and the radar line of sight (LOS). The reference coordinates are defined as O-XYZ and the origin O is located at the centroid The Z-axis is along the precession axis, and the LOS of the radar is set in the XOZ plane. The local coordinates are defined as O'-xyz and the origin O' is located at the centre of the base of a cone-shaped target, and the z-axis is along the target symmetry axis. A monostatic radar is located at Tx and the bistatic receiver is located at Rx. γ_T and ϕ_T denote the elevation angle and the azimuth angle of the LOS of the monostatic radar ($\angle T_x OZ$), respectively. γ_R and ϕ_R denote the elevation angle ($\angle R_x OZ$) and the azimuth angle of the LOS of the bistatic receiver, respectively. h denotes the target height, and r denotes the radius of the base. b denotes the range between the origin O and the center of the base. θ and ϕ_0 denote the elevation ($\angle AOZ$) and azimuth angles of the target axis, respectively.
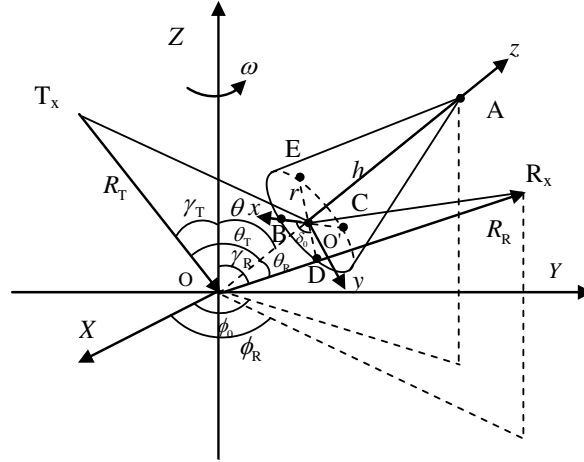

Figure 1. HRRP sequences from electromagnetic calculation data.

The angle between the LOS of the transmitter and the target axis ($\angle T_x OA$), which is denoted by θ_T, at time t satisfies

$$\cos \theta_T = \cos \theta \cos \gamma_T + \sin \theta \sin \gamma_T \cos (\omega t + \phi_0). \tag{1}$$

The angle between the LOS of the receiver and the target axis ($\angle R_x OA$), which is denoted by θ_R, satisfies

$$\cos \theta_R = \cos \theta \cos \gamma_R + \sin \theta \sin \gamma_R \cos (\omega t + \phi_0 - \phi_R). \tag{2}$$

The bistatic angle β satisfies

$$\cos \beta = \cos \gamma_T \cos \gamma_R + \sin \gamma_T \sin \gamma_R \cos \phi_R. \tag{3}$$

$$\cos \beta/2 = \sqrt{\frac{1 + \cos \gamma_T \cos \gamma_R + \sin \gamma_T \sin \gamma_R \cos \phi_R}{2}}. \tag{4}$$

In the real scene, the bistatic angle can be obtained by solving triangle geometry of transmitter, target and receiver, while the target is under tracking.

According to the spatial geometry, the azimuth angle of the LOS of the receiver in the local ordinates (i.e., φ_R in Fig. 1) can be approximated by the following expression[15].

$$\cos \varphi_R \approx \frac{\cos \beta - \cos \theta_T \cos \theta_R}{\sin \theta_T \sin \theta_R} \tag{5}$$

For the far field, the bistatic distance of each scattering centre from the reference centre O is defined as follows.

$$\begin{cases} \Delta R_{S_A} \approx -2 \cos (\beta/2) (b + h) \cos \theta_{Bi} \\ \Delta R_{S_D} \approx -2 \cos (\beta/2) (b \cos \theta_{Bi} + r \sin \theta_{Bi}) \\ \Delta R_{S_E} \approx -2 \cos (\beta/2) (b \cos \theta_{Bi} - r \sin \theta_{Bi}) \end{cases} . \tag{6}$$

where ΔR_{S_A}, ΔR_{S_D}, and ΔR_{S_E} denote the bistatic distances of scattering centers A, D and E from the reference centre O, respectively, from the reference center.

If $\theta_R = \theta_T, \phi_R = \phi_T$, Eq. (7) corresponds to the monostatic case, which can be expressed as

$$\begin{cases} \Delta R_{M_A} \approx -2 (b + h) \cos \theta_T \\ \Delta R_{M_B} \approx -2 (b \cos \theta_T + r \sin \theta_T) \\ \Delta R_{M_C} \approx -2 (b \cos \theta_T - r \sin \theta_T) \end{cases} . \tag{7}$$

where ΔR_{M_A}, ΔR_{M_B}, and ΔR_{M_C} denote the distances to scattering centers A, B and C, respectively, from the reference center.

The bistatic micro-Doppler corresponding to each bistatic scattering center can be expressed as

$$\begin{cases} f_{S_A} \approx -\frac{\omega}{\lambda} (b + h) \sin \theta \left[\sin \gamma_T \sin (\omega t + \phi_0) + \sin \gamma_R \sin (\omega t + \phi_0 - \phi_R) \right] \\ f_{S_D} \approx -\frac{\omega}{\lambda} \sin \theta \left[\sin \gamma_T \sin (\omega t + \phi_0) + \sin \gamma_R \sin (\omega t + \phi_0 - \phi_R) \right] \left[b - r \frac{\cos \theta_T + \cos \theta_R}{\sqrt{2 + 2 \cos \beta - (\cos \theta_T + \cos \theta_R)^2}} \right] \\ f_{S_E} \approx -\frac{\omega}{\lambda} \sin \theta \left[\sin \gamma_T \sin (\omega t + \phi_0) + \sin \gamma_R \sin (\omega t + \phi_0 - \phi_R) \right] \left[b + r \frac{\cos \theta_T + \cos \theta_R}{\sqrt{2 + 2 \cos \beta - (\cos \theta_T + \cos \theta_R)^2}} \right] \end{cases} . \tag{8}$$

And the monostatic micro-Doppler corresponding to each monostatic scattering center can be expressed as

$$\begin{cases} f_{m,A} \approx -\frac{2\omega}{\lambda} (b + h) \sin \theta \sin \gamma_T \sin (\omega t + \phi_0) \\ f_{m,B} \approx -\frac{2\omega}{\lambda} \sin \theta \sin \gamma_T \sin (\omega t + \phi_0) \left(b - r \frac{\cos \theta_T}{\sqrt{1 - \cos^2 \theta_T}} \right) \\ f_{m,C} \approx -\frac{2\omega}{\lambda} \sin \theta \sin \gamma_T \sin (\omega t + \phi_0) \left(b + r \frac{\cos \theta_T}{\sqrt{1 - \cos^2 \theta_T}} \right) \end{cases} . \tag{9}$$

From Eq. (10), it can be obtained that the monostatic and bistatic micro-Dopplers corresponding to the scattering center A obey the sinusoidal rule while the monostatic and bistatic micro-Dopplers corresponding to the scattering centers on the edge of the bottom surface are more complex. Especially, the bistatic micro-Doppler is related with the LOS angles of two stations and bistatic angle, so it is highly nonlinear. If the traditional RD algorithm is used for this type target imaging, it is unable to get a clear image.

3. SCALING OF MONOSTATIC AND BISTATIC RID IMAGES

3.1. Monostatic and Bistatic RID Imaging

Assuming that the linear frequency modulated (LFM) signal is used by the transmitter and that the transmitted signal is used as the reference signal by the receiver with a delay time, the bistatic high range resolution profile (HRRP) sequence of the target can be obtained via stretch processing and range compressing as follows.

$$S_B(r,\tau) = T_P \sum \sigma_{B,i} \text{sinc}\left[\frac{B}{c}\left(r - \Delta R_{S_i}(\tau)\right)\right] e^{-j\frac{2\pi}{\lambda}\Delta R_{S_i}(\tau)}. \tag{10}$$

where T_p and B represent the pulse width and the chirp rate; c is the light speed; λ is wave length; $\sigma_{B,i}$ is bistatic RCS; ΔR_{S_i} denotes the bistatic distance of the ith scattering centre from the reference centre, $i = A, D, E$.

The monostatic HRRP sequence can be expressed as

$$S_M(r,\tau) = T_P \sum \sigma_{M,i} \text{sinc}\left[\frac{B}{c}\left(r + \Delta R_{M_i}(\tau)\right)\right] e^{-j\frac{2\pi}{\lambda}\Delta R_{M_i}(\tau)}. \tag{11}$$

where $\sigma_{M,i}$ is the monostatic RCS, and ΔR_{M_i} denotes the bistatic distance of the ith scattering centre from the reference centre, $i = A, B, C$.

From the monostatic and bistatic HRRP sequence expressions, it can be obtained that the phase of time sequence corresponding to each distance r contains corresponding distance items of various scattering centers: $\frac{2\pi}{\lambda}\Delta R_{M_i}(\tau)$ and $\frac{2\pi}{\lambda}\Delta R_{S_i}(\tau)$. Taking time-frequency analysis on this time series, micro-Doppler corresponding to each scattering center can be obtained. The amplitudes corresponding to some scattering centers are strong in certain distance, while some other scattering amplitudes are weak.

Due to high-speed precession and small precession angle of target, the enough resolution cannot be obtained in a short time by cross compression, while range cell migration will happen with a long time observation, and fuzzy will appear with cross compression. So the time-frequency analysis method is used for RID imaging at each time as [12], the imaging process of time-frequency analysis is described as follows.

Firstly, getting HRRP sequence as a time-range distribution matrix after motion compensation $S(r,\tau)$ $(M \times N)$.

Then, Taking time-frequency transformation on the time sequence on the same distance cell, the time-frequency distribution matrix $(N \times L)$ of different distance units is obtained.

Finally, obtaining the dimensional matrix $(M \times N \times L)$ with distance-time-instantaneous Doppler by arranging the above time-frequency distribution matrixes, and getting the two-dimensional RID image $(M \times L)$ at different moments.

Although there are many methods of time-frequency analysis, the smoothed pseudo Wegener Ville distribution (SPWVD) is used in this paper in order to meet the high time-frequency resolution requirement and suppress the cross terms, where the sampling frequency is two times of short-time Fourier transform (STFT) method. Both the monostatic and bistatic RID image sequence can be obtained by taking time-frequency transformation on the monostatic and bistatic range profile sequence, respectively.

3.2. Scaling of RID Images

According to the monostatic and bistatic scattering characteristics of cone-shaped target, although the scattering centers observed by two receivers are not the same, they are all on the vertex and edges of bottom. Due to the rotary symmetry characteristics, the two-dimensional images after scaling observed in all directions should have the same size. Assume that two non-scaled RID images A and B have been obtained by T/R-R bistatic radar at the same time, which have the proportional relation with the scaled target image C. Taking expansion of the image A along the cross direction(scaling factor is set as a), the image A can be mapped to the actual scaled image C. For the bistatic RID image B Taking expansion of the image A along the cross direction with scaling factor b and the rotation transform

with angle ϕ, the image B can be mapped to the actual scaled image C. The transform process can be described as the coordinate's transformation of any strong scattering point in the image and expressed as follows.

$$\begin{pmatrix} a & 0 \\ 0 & 1 \end{pmatrix} \begin{pmatrix} x_M \\ y_M \end{pmatrix} = \begin{pmatrix} \cos\phi & -\sin\phi \\ \sin\phi & \cos\phi \end{pmatrix} \begin{pmatrix} b & 0 \\ 0 & 1 \end{pmatrix} \begin{pmatrix} x_B \\ y_B \end{pmatrix}. \tag{12}$$

where (x_M, y_M) and (x_B, y_B) represent the strong scattering points extracted from the monostatic and bistatic RID images, respectively, and both of them correspond to the same or equivalent place of the target. This equation can also be transformed as follows:

$$\begin{pmatrix} x_M \\ y_M \end{pmatrix} = \begin{pmatrix} \dfrac{b}{a}\cos\phi & -\dfrac{1}{a}\sin\phi \\ b\sin\phi & \cos\phi \end{pmatrix} \begin{pmatrix} x_B \\ y_B \end{pmatrix} \tag{13}$$

In order to scaling both images, the key problem is to estimate the parameters a and b. If the coordinates of at least two pairs of scattering centers are known, the above parameters (a, b, ϕ) can be estimated by solving the equations. Assume that K ($K \geq 2$) pairs of scattering centers extracted from images A and B have been associated correctly, and they are represented as (x_{M_i}, y_{M_i}), (x_{B_i}, y_{B_i}), $i = 1, 2, \ldots K$, then a cost function can be constructed as follows

$$f(a, b, \phi) = \sum_i^K \left\| \begin{pmatrix} x_{M_i} \\ y_{M_i} \end{pmatrix} - \begin{pmatrix} \dfrac{b}{a}\cos\phi & -\dfrac{1}{a}\sin\phi \\ b\sin\phi & \cos\phi \end{pmatrix} \begin{pmatrix} x_{B_i} \\ y_{B_i} \end{pmatrix} \right\|^2. \tag{14}$$

Then, the parameter estimation problem is transformed as the optimization problem with constraint conditions. When the function achieves the minimum value, the optimal values of the three parameters are obtained. Because it is difficult to obtain analytical solutions, the least squares algorithm can be used and the optimal solution of equation can be obtained by iterative optimization. At the same time, an initial value should be given by the following way, and the algorithm will converge quickly because the initial value is close to the true value.

Suppose that the coordinates of two pairs of scattering centers in the image A and B are extracted as (x_{M_1}, y_{M_1}), (x_{B_1}, y_{B_1}), (x_{M_2}, y_{M_2}), (x_{B_2}, y_{B_2}) respectively, the following equations can be obtained by substitute them into Eq. (14).

$$\begin{pmatrix} x_{M_1} \\ y_{M_1} \\ x_{M_2} \\ y_{M_2} \end{pmatrix} = \begin{pmatrix} x_{B_1} & y_{B_1} & 0 & 0 \\ 0 & 0 & x_{B_1} & y_{B_1} \\ x_{B_2} & y_{B_2} & 0 & 0 \\ 0 & 0 & x_{B_2} & y_{B_2} \end{pmatrix} \begin{pmatrix} \dfrac{b}{a}\cos\phi \\ -\dfrac{1}{a}\sin\phi \\ b\sin\phi \\ \cos\phi \end{pmatrix}. \tag{15}$$

This equation has the only solution on condition that the coefficient matrix is reversible, i.e., the determinant is not zero. So

$$x_{B_1} y_{B_2} - x_{B_2} y_{B_1} \neq 0. \tag{16}$$

where it means that the two points selected should not be zero points, and the slopes of both lines connection to the origin should not be the same, thus the angle between the both lines should be large. Then the scaling procedure of monostatic and bistatic RID images can be given as follows.

Step 1) Obtaining the monostatic and bistatic RID sequences
To get the monostatic and bistatic RID sequences by using joint time-frequency transform method on monostatic and bistatic radar echo after motion compensation, and choose the monostatic and bistatic RID images at the same time. To scale the monostatic RID image with resolution $c/2B$ in both range and cross distance calibration, and bistatic RID images with resolution $c/2B\cos(\beta/2)$.

Step 2) Extraction of scattering centers
Due to the limited resolution, each scattering center in the RID image is usually not a point but a certain peak area. More accurate scattering center location can be obtained by threshold detection and clustering.

Step 3) Matching of scattering centers
Scattering center association is a hard problem in the bistatic observation, and it is very difficult to match the scattering centers without prior information. Fortunately, the target attitude can be estimated roughly by tracking and narrowband feature extraction, and the attitude difference between two images can be estimated roughly according to the bistatic angle, then the scattering center association can be achieved by manually selecting points.

Step 4) Solving the initial values by using two scattering centers.
The initial value of a, b, ϕ can be obtained by substituting the position parameters of two pairs of associated scattering centers into Eq. (16).

Step 5) Solving the optimal value using the least squares method with multiple pairs of scattering centers.
Substituting the initial values of a, b, ϕ and parameters of multiple pairs of scattering centers into Eq. (12), the optimal value of a, b, ϕ can be solved by Gauss-Newton iterative method.

Step 6) Scaling monostatic and bistatic RID images
According to the parameters obtained from the solution, the cross scaling of monostatic and bistatic RID images are performed with scale factors $a \cdot c/2B$ and $b \cdot c/2B \cos(\beta/2)$, respectively.

In order to achieve more accurate cross scaling, the same monostatic RID image can be used to match several bistatic RID images, and then the final scale factor can be obtained by averaging. Similarly, the same bistatic RID image can be used to match several monostatic RID images. It is noted that there are micro-Dopplers of some scattering centers are nearby zero, and the RID images are not high quality at that time. So the image contrast should be calculated firstly and those images with high image contrast can be used for image scaling.

4. DYNAMIC SIMULATION AND ANALYSIS

A conductive model was constructed using FEKO software to verify the previously described analysis using the parameters shown in Fig. 2. According to the target structure, three monostatic scattering centers are marked as A, B and C, and the bistatic scattering centers are marked as D and E. The reference center of the target is set to point O. The electromagnetic calculation parameters are listed in Table 1. A four-dimensional complex matrix $\mathbf{D}_{M \times N \times P \times Q}$ (M is the number in the incident direction, N and P represent the numbers in the scattering direction, Q is the frequency number) is calculated with the multilevel fast multipole method. Here, $M = 901$, $N = 901$, $P = 901$, $Q = 101$.

The simulation parameters are as follows: $\theta = 10°$, $\omega = 2\pi$ rad/sec, $\phi_0 = 0°$, $\gamma_T = 40°$, $\gamma_R = 100°$, $\phi_R = 0°$ and the bistatic angle is calculated as $60°$. The pulse repetition frequency is 500 Hz, and 1000 pulses are observed. In the simulation scene, these angles (θ_T, θ_R, and φ_R) change with the target's precession and are calculated via equations ballistic (5) in series. Then, the monostatic and bistatic scattering coefficients that correspond to (θ_T, θ_R, φ_R) are extracted from the data matrix. The additive
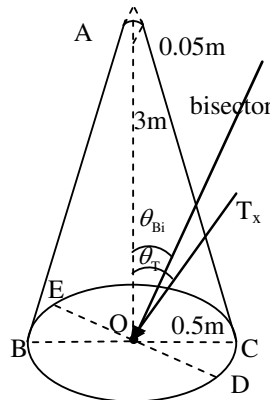

Figure 2. Target model for electromagnetic calculation.

Table 1. Electromagnetic calculation parameters.

Parameter	Unit	Value
Start frequency	GHz	9.5
End frequency	GHz	10.5
Frequency interval	MHz	10
Incident elevation	deg	0~180
Scattering elevation	deg	0~180
Scattering azimuth	deg	0~180
Angle interval	deg	0.2
Incident polarization		horizontal
Receiving polarization		horizontal

white Gauss white noises are added to the bistatic scattering coefficients in the frequency field. The monostatic and bistatic HRRPs are obtained by taking the Inverse Fast Fourier Transform (IFFT) of the data in the frequency field and arranging it by a slow-time sequence, which constructs the time-range distribution matrix as shown in Fig. 3.

Figure 3(a) shows the monostatic time-range distribution constructed by the monostatic HRRP sequence, where two scattering centers can be observed from the vertex and bottom edge of the cone, respectively. Fig. 3(b) shows the bistatic time-range distribution constructed by the bistatic HRRP sequence, where two scattering centers can be observed from the vertex and bottom edge of the cone, respectively. It can be seen that the monostatic and bistatic HRRPs are different from each other.
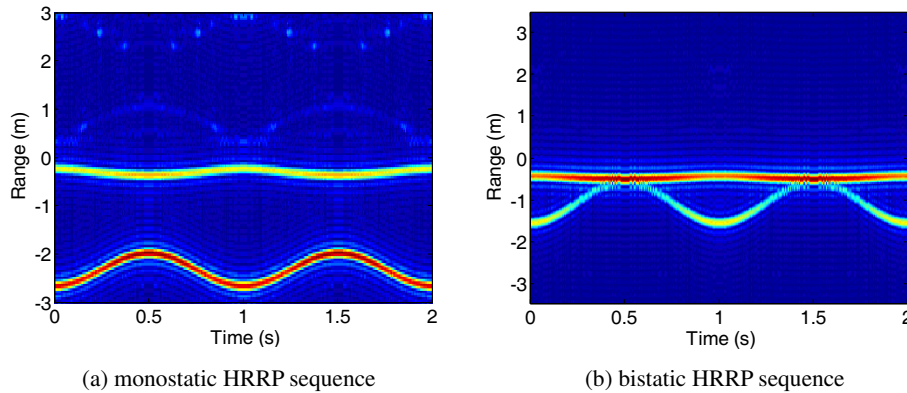

(a) monostatic HRRP sequence   (b) bistatic HRRP sequence

Figure 3. HRRP sequences from electromagnetic calculation data.

Figure 4 shows the monostatic and bistatic RID images at some time, and only two scattering centers can be seen due to target occlusion. The scattering center on vertex is not an ideal point and slides on the surface, so the monostatic RID image is not focused very well. In bistatic RID image, the scattering intensity of the cone vertex is significantly less than the bottom edge, which makes great different between the monostatic and bistatic RID images. The positions of the two scattering centers are extracted from monostatic and bistatic RID images firstly, and they are associated with each other. Then, the expansion coefficients a and b are solved as $a = 0.121$, $b = 0.093$ through optimal iterative search. Finally, the scaling factors of monostatic and bistatic RID images are estimated as 0.014 and 0.018, respectively. The scaled images are shown in Fig. 5, and the solid line in the figure represents target contour at the current time. It can be seen that the scattering centers are almost on the target contour, which illustrates that the two-dimensional image after scaling can reflect the real size of the target.
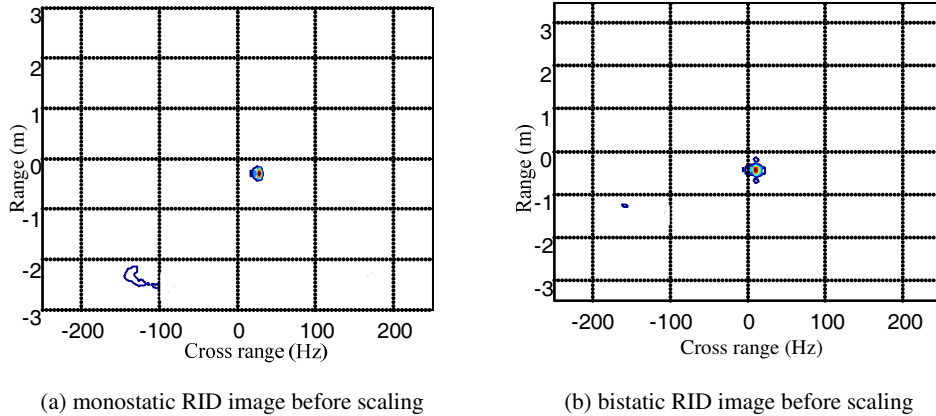
(a) monostatic RID image before scaling

(b) bistatic RID image before scaling

Figure 4. Monostatic and bistatic RID images.

(a) monostatic image after scaling

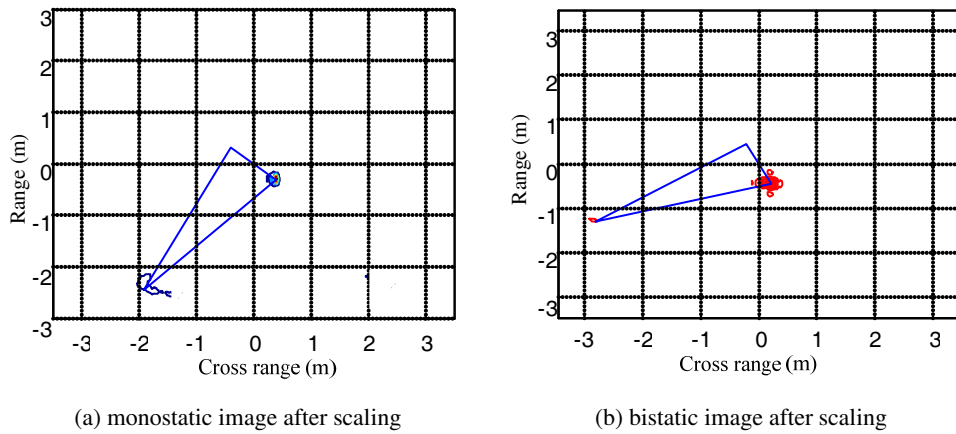(b) bistatic image after scaling

Figure 5. Two-dimensional image after scaling.

5. CONCLUSIONS

The method of time-frequency transform is used for T/R-R complex bistatic radar imaging of precession targets, and the monostatic and bistatic RID images are scaled through image match with the rotational symmetry characteristics. The scaled monostatic and bistatic images can reflect the real target size and can be used for target recognition directly. More abundant and stable target information can be obtained, which expand the ability of the monostatic radar. The method is also suitable for spinning, wobbling, nutation and other micro-motion targets. For those ballistic targets with a tail, the signal corresponding to the target main body should be separated from the signal corresponding to the target tail, then the proposed method can be used to obtain the scaled image of the target main body.

ACKNOWLEDGMENT

REFERENCES

1. Wang, T., X. Wang, et al., "Estimation of precession parameters and generation of ISAR images of ballistic missile targets," *IEEE Transactions on Aerospace and Electronic Systems*, Vol. 46, No. 4, 1983–1995, 2010.

2. Zhuang, Z., X. Wang, X. Li, et al., *Radar Target Recognition*, 311–388, Higher Education Press, Beijing, 2015.

3. Vespe, M., C. Baker, et al., "Radar target classification using multiple perspectives," *IET Radar Sonar Navigation*, Vol. 1, No. 4, 300–307, 2007.

4. Zhu, F., X.-D. Zhang, et al., "Nonstationary hidden markov models for multiaspect discriminative feature extraction from radar targets," *IEEE Transactions on Signal Processing*, Vol. 55, No. 5, 2203–2214, 2007.

5. Ye, C.-M., J. Xu, et al., "Key parameter estimation for radar rotating object imaging with multi-aspect observations," *Science in China: Information Sciences*, Vol. 53, No. 8, 1641–1652, 2010.

6. Bai, X., F. Zhou, M. Xing, and Z. Bao, "Scaling the 3-D image of spinning space debris via bistatic inverse synthetic aperture radar," *IEEE Transactions on Geoscience Remote Sensing Letters*, Vol. 7, No. 3, 430–434, 2010.

7. Zhang, Y.-B., Z.-B. Zhu, Z.-Y. Tang, et al., "Bistatic inverse synthetic aperture radar image formation," *Journal of Electronics & Information Technology*, Vol. 28, No. 6, 969–972, 2006.

8. Chen, V. C., A. des Rosiers, and R. Lipps, "Bi-static ISAR range-doppler imaging and resolution analysis," *2009 IEEE Radar Conference*, 1–5, Pasadena, California, United States, 2009.

9. Martorella, M., J. Palmer, J. Homer, et al., "On bistatic inverse synthetic aperture radar," *IEEE Transactions on Aerospace and Electronic Systems*, Vol. 43, No. 3, 1125–1134, 2007.

10. Martorella, M., "Analysis of the robustness of bistatic inverse synthetic aperture radar in the presence of phase synchronization errors," *IEEE Transactions on Aerospace and Electronic Systems*, Vol. 47, No. 4, 2673–2689, 2011.

11. Pastina, D., M. Bucciarelli, and P. Lombardo, "Multistatic and MIMO distributed ISAR for enhanced cross-range resolution of rotating targets," *IEEE Transactions on Geoscience and Remote Sensing*, Vol 48, No. 8, 3300–3318, 2010.

12. Chen, V. C. and H. Ling, *Time-Frequency Transforms for Radar Imaging and Signal Analysis*, 1st edition, 1–6, Artech House, Norwood, MA, 2002.

13. Jin, G.-H., X.-Z. Gao, X. Li, et al., "ISAR image cross scaling method for ballistic target based on image registration," *Systems Engineering and Electronics*, Vol. 32, No. 12, 2565–2569, 2012.

14. Ai, X. F., X. H. Zou, Y. Z. Li, et al., "Bistatic scattering centres of cone-shaped targets and target length estimation," *Science China: Information Sciences*, Vol. 55, No. 12, 2888–2898, 2012.

15. Ai, X. F., X. H. Zou, J. Liu, et al., "Bistatic high range resolution profiles of precessing cone-shaped targets," *IET Radar Sonar Navigation*, Vol. 7, No. 6, 615–622, 2013.